Accepted Manuscript

Plasmonic polyaniline/gold nanorods hybrid composites for selective NIR photodetection: Synthesis and characterization

Gaser N. Abdelrasoul, Francesca Pignatelli, Ioannis Liakos, Roberto Cingolani, Athanassia Athanassiou

PII: S1359-8368(18)30651-6

DOI: 10.1016/j.compositesb.2018.05.015

Reference: JCOMB 5685

To appear in: *Composites Part B*

Received Date: 28 February 2018

Revised Date: 28 April 2018

Accepted Date: 9 May 2018

Please cite this article as: Abdelrasoul GN, Pignatelli F, Liakos I, Cingolani R, Athanassiou A, Plasmonic polyaniline/gold nanorods hybrid composites for selective NIR photodetection: Synthesis and characterization, *Composites Part B* (2018), doi: 10.1016/j.compositesb.2018.05.015.

Plasmonic Polyaniline/Gold Nanorods Hybrid Composites for selective NIR photodetection: synthesis and characterization

Gaser N. Abdelrasoul[1,2*], Francesca Pignatelli[1], Ioannis Liakos[3], Roberto Cingolani[1], Athanassia Athanassiou[1]

1. Smart Materials, Department of Nanophysics, Istituto Italiano di Tecnologia, via Morego 30, 16163 Genova, Italy.
2. Forensic Sciences and Medicolegal Authority, Cairo, Egypt.
3. Center for Micro-BioRobotics, Istituto Italiano Di Tecnologia, Via Morego 30, 16163 Genova, Italy.

Abstract:

Abstract scheme

In this study, we present the development of polyaniline/gold nanorod nanocomposites and the effect of the nanorods' aspect ratio and concentration on the overall electrical conductivity of nanocomposite systems. The electrical characterization showed that at the same atomic gold concentration, the conductivity of the nanocomposites increased by about 14 % after increasing the gold nanorods' aspect ratio from 2.9 to 3.8. Furthermore, the conductivity of the nanocomposites increases linearly with the concentration of atomic gold, keeping the nanorods' aspect ratio stable, due to increasing the metallic content. The interaction between polyaniline and gold nanorods was investigated by FTIR, micro Raman, and XPS spectroscopic techniques, indicating the delocalization of the charges across the polymer chains induced by the incorporation of the nanorods. The interaction most likely occurs through the imine nitrogen of the polymer's backbone. The homogenous distribution of the gold nanorods in the polyaniline matrix was verified by TEM. Furthermore, the selective photosensitivity of the developed nanocomposites to NIR light was examined, and an increase in their current density was detected when the nanocomposites were irradiated at the wavelength that coincides with the longitudinal plasmonic resonance absorption of the incorporated nanorods. We foresee applications of the developed nanocomposites in numerous optoelectronic sectors.

Keywords: Polyaniline – Gold nanorods – Nanocomposites – Photodetectors – Polyaniline/gold nanorods composites.

Introduction

Polymeric nanocomposites have attracted considerable attention for applications in many technological areas, since they combine the lightweight, low cost and processability of polymeric materials with the characteristic properties of the embedded inorganic nanoparticles, e.g. conductivity or sensitivity to external stimuli, etc. The interaction between the nanocomposite components can be either physical or chemical depending on the surface nature of the nanoparticles and the presence of functional groups on the polymer chain. Among the various developed nanocomposite systems, the ones used most extensively in the field of flexible optoelectronics are the conductive polymer/metallic nanoparticle composites, due to the charge transfer processes occurring at the interface of the nanoparticles with the matrix.

Conductive polymer polyaniline (PANI) has received particular attention due to its magnificent properties such as good stability at ambient environmental conditions, simple and versatile preparation methods and its low cost. Various researchers have employed PANI in several application fields, such as anti-corrosive coatings [1], conductive polymer composites [2-5], drug delivery [6] and sensors [7-9]. PANI is synthesized by oxidation of aniline in an acidic medium either chemically[10] or electrochemically [11, 12]. PANI is an organic semiconductor and its π-conjugation structure is responsible for its electrical conductivity either through oxidation-reduction reactions or acid doping processes. Its band gap corresponds to the energy required to excite one electron from the HOMO (Highest Occupied Molecular Orbital) to the LUMO (Lowest Unoccupied Molecular Orbital). Through camphor sulfonic acid (CSA) doping of PANI, charge transfer is induced along the polymeric chain by protonation of imine nitrogen sites [13]. When a vacancy form, one electron from the HOMO orbital is relocated to the LUMO level, resulting in a localized polaron. Under an external electric field, polarons step to neighboring trapping centers, resulting in the electrical conduction of the polymer. In general, the conductivity of the polymer is restricted by the unusual contacts between different crystalline domains limiting the polarons ability to jump from one chain to the next. Diverse nanomaterials as carbon nanotubes [14-16], titanium oxide [17-19], cadmium sulfide [20-23], metallic nanoparticles [24-26] and graphene [27] with different size and shapes have been incorporated in PANI, producing nanocomposites with controllable properties, depending on the nature of the nanofillers and their interaction with the polymeric matrix. These nanocomposites were explored in different application fields including biology [28], memory devices [29], electrocatalysis [30, 31], biosensors [32] and electronics [33]. The merger of polyaniline with metallic nanoparticles to form composites has been attempted so far by diverse methodologies [34, 35]. Some of the efficient strategies included are physical mixing [36-38], layer by layer deposition [39], polymerization of aniline in the presence of nanoparticles [40], the growth of metallic nanoparticles over the PANI chains [41], and finally, the polymerization of aniline combined with the nucleation and growth of metallic nanoparticles [42]. Direct mixing gives a simple route for preparing PANI composites with excellent control over the ratio of each component. The shape and size of each individual component can be well designed before mixing. Furthermore, the physical blending of PANI solution with nanoparticle dispersions prevents severe structural deformation of the embedded nanoparticles that can happen in the case of in-situ polymerization due to the extremely low pH of the polymerization reaction solution.

PANI hybridized with spherical gold nanoparticles as metallic nanofillers was already used in order to enhance the electrical conductivity and extend the diversity of PANI's applications [37, 38]. The enhancement of the electrical conductivity of the resulting nanocomposites is usually explained by the increase of the charge density and charge mobility. Under adequate applied voltage, electrons located in imine nitrogens of PANI were proposed to gain enough energy to overcome the interface between the polymer and gold nanoparticles [24]. Gold nanoparticles have Fermi levels close to the HOMO level of PANI. Therefore, gold nanoparticles abstract one of the pair electrons located at the nitrogen atom in the HOMO level in order to transfer it to the LUMO level. Consequently, gold nanoparticles can be employed as dopants, enhancing the conductivity of the PANI even at lower acidic doping levels. The structural morphology of both PANI and gold nanoparticles, as well as the capping agent used, determine the kind of interaction between gold nanoparticles and PANI, which deeply affects the interfacial region and hence the transfer of charge [43]. The morphology and the size of metallic nanoparticles incorporated into the PANI are expected to play a crucial role in the properties of the resulting nanocomposites. To the best of our knowledge, no investigation regarding the effect of the gold nanoparticle's morphology on the properties of the polyaniline composites was previously reported.

Gold nanorods (AuNRs) have interesting properties owing to their anisotropic structure, which has attracted much attention for potential use in several applications. The optical and electronic properties of AuNRs depend on their aspect ratio (length/width) [44-46], surface functionality [47, 48] and the dispersed medium [49, 50]. AuNRs are characterized by dual surface plasmonic absorption peaks, both longitudinal and transversal, corresponding to the oscillation of free electrons along the longitudinal and transversal axes of the nanorods, respectively. Therefore, the incorporation of AuNRs of different aspect ratios into PANI is expected to add novel interesting properties to the nanocomposite materials.

Here we investigate the interaction of photochemically synthesized AuNRs with PANI of 65 kDa doped with Camphor sulfonic acid (CSA). In particular, we first focus on the effect of the nanorods' concentration and aspect ratio on the conductivity of the nanocomposites. AuNRs with three different aspect ratios, from 2.5 up to 3.8, were separately embedded into the PANI matrix and characterized. The homogeneous distribution of AuNRs in the PANI matrix was investigated by transmission electron microscopy (TEM). The electrical conductivity of the PANI and of the nanocomposite films was measured using the transmission line technique. The alterations in the optical properties of PANI nanocomposites, due to the different AuNRs used, were monitored by UV-Vis spectroscopy. FT-IR and micro Raman spectroscopy were employed in order to evaluate the interaction between AuNRs and PANI chains. Furthermore, X-ray photoelectron spectroscopy was used to characterize the chemical bonds in the composites. Exploiting the surface plasmon resonance induced local field enhancement, we designed a photodetector sensitive to specific wavelengths in the infrared region. The sensitivity and the detection limit of the photodetector were determined.

Experimental

Materials

Hydrogen tetrachloroaurate trihydrate ($HAuCl_4.3H_2O$) (Alfa aesar 99.99%), Cetyltrimethylammonium bromide (CTAB) (Fluka ≥99%), Silver nitrate $AgNO_3$ (Aldrich 99.9999%), Ascorbic acid (AA) (Sigma-Aldrich ACS reagent 99%), Cyclohexane (TCI, 99%), and Acetone (Sigma-Aldrich ≥99.9%) were employed without any further purification. PANI of molecular weight 65KD and camphor sulfonic acid (CSA) (Sigma Aldrich) were used as received. N, N Dimethylformamide (DMF) (San Carlos 99%) was used as received as a solvent for polyaniline. High purity Milli Q water (18.2 MΩ) was used for the preparation of AuNRs dispersion solutions in all experiments.

Methods

I. AuNRs synthesis: AuNRs were synthesized via the photochemical technique as previously reported with some modifications [51-54]. First, 0.2 mL of AA (40 mM) was pipetted into three different AuNR growth solutions prepared by the sequential mixing of 0.25 mL of $HAuCl_4.3H_2O$ (24 mM), 3mL of CTAB (80mM), 0.065 mL of acetone, 0.045 mL of cyclohexane, and finally three different amounts of $AgNO_3$ (10 mM) [0.04, 0.07, 0.1 mL]. The precursor solutions were incubated in the dark for 3 hours prior to UV irradiation with a UV lamp (λ = 254 nm) for 30 minutes. At the end of the reaction, the color of the growth solution changes from colorless to green, brown, or reddish brown depending on the aspect ratio of the resulting NRs. The color of the gold nanorods attributes to the aspect ratio and the maximum plasmonic absorption of the nanorods. As the aspect ratio of the gold nanorods increases, their maximum plasmonic absorption redshifts and so the color of the nanorods dispersion solution change from colorless to different colors based on their aspect ratios. Where the nanorods of aspect ratio 2.5 its dispersion solution is green, and

the nanorods of aspect ratios 2.9 and 3.8 their dispersion solutions are brown, and reddish brown, respectively. Finally, the AuNR solutions were centrifuged once at 4000 rpm for 10 minutes to separate large gold clusters. The resulting supernatant was collected and centrifuged at 14000 rpm for 20 minutes. This was repeated twice to separate the excess of CTAB and the unreacted materials from the solution. The supernatant was exchanged with distilled water each time. 20 µL of the AuNR dispersions were deposited over carbon coated copper grid for TEM investigation. The resulting value of Au ion concentration obtained by ICP measurements and the dimensions of AuNRs, measured from TEM micrographs, were used to estimate the concentration of AuNRs. The AuNRs used for the preparation of the nanocomposites have aspect ratios of 2.5, 2.9 and 3.8.

II. PANI/CSA-ES preparation(PANI/CSA-ES-ES): A 0.5 wt% PANI solution was prepared by dissolving 0.075 g of PANI in 14.925 g of DMF. The solution was stirred for 24 hours, and then 0.15 g of CSA was added to the PANI solution. The PANI/CSA-ES Emeraldine Salt (PANI/CSA-ES-ES) solution was stirred for another 24 hours, then filtrated twice using filter paper with pore sizes of 0.2 µm. 1 mL of the final filtrated PANI/CSA-ES-ES solution was dried and weighed in order to evaluate the final concentration of PANI/CSA-ES in the solution after double filtration. The final concentration of PANI/CSA-ES-ES in DMF solution was 4 mg/mL. The pH of the PANI/CSA-ES-ES solution was 4.35.

III. PANI/CSA-ES-AuNRs Nanocomposites Preparation: The composition and the concentration of the components of the prepared nanocomposite films are summarized in Table 1. Briefly, a specific amount of AuNRs dispersed in water was mixed with a certain volume of PANI/CSA-ES solution (2 mg/ml concentration) to obtain a total volume of 1 ml. The nanocomposite solutions were sonicated for 1 hour. An aliquot of each nanocomposite solution was drop cast over different substrates including glass, silicon wafer, and a microelectrode array containing gold square electrodes sputtered over a silicon substrate with a thickness of 100 nm, for further investigation. The gold square electrodes each have an area of 100 μm^2. The thickness of the polymer and nanocomposite layer was adjusted to be 0.2 µm by controlling the drop casting process and measured with a profilometer (AMBIOS XP2 Technology) through applying a probe with a pressure force of 0.1 mg/mm^2 along a 5 mm scanning distance.

Table 1: the composition of each PANI/CSA-ES-AuNRs used in the study.

Composite Name	Volume of PANI/CSA-ES solution (µl)	AuNRs aspect ratio	AuNRs Concentration (nM)	Au Concentration [Au] (ppm)	Au percentage (wt %)
Comp I	900	2.5	65	2.6	0.130
Comp II	965	2.9	65	2.0	0.100
Comp III	938	3.8	65	1.9	0.095
Comp IV	917	3.8	87	2.6	0.130
Comp V	866	2.5	87	3.4	0.170

Characterizations

A Jeol Electron Microscope (JEM 1011) operating at 100 KV was used for transmission electron microscope (TEM) measurements of the AuNRs and nanocomposites. A 20 µL solution of both AuNR dispersion and nanocomposites were drop casted over a carbon-coated copper TEM grid of 300 meshes and dried at room temperature.

The optical absorption investigations were carried out with a Varian Cary 6000i UV-Vis-NIR spectrophotometer. For collecting the optical absorption spectra, 200 µL of the PANI/CSA-ES-ES and nanocomposite solutions were separately deposited and then dried over a clean glass slide substrate. After drying the polymer and nanocomposites films, their spectra were measured using a clean glass slide as a reference. Fourier-Transformed Infrared (FT-IR) spectra of conductive PANI and the nanocomposites were performed by a Bruker Vertex 70v FT-IR instrument in transmission mode. The Spectra were collected under a vacuum in the range of 500-4000 cm^{-1} at a resolution of 4 cm^{-1} using a DTGS detector. Polymer and nanocomposite films deposited on glass substrates were used for measuring the FTIR spectra. X-ray photoelectron spectroscopy (XPS) measurements were made using a Specs Lab2 electron spectrometer with a monochromatic X-ray source radiation at 1253 eV and equipped with a Phoibos analyzer Has 3500 (Emispherical Energy Analyzer). The applied voltage of the Mg Kα X-ray source was 10 kV and the applied current was 15 mA. The pressure in the analysis chamber was approximately 2 x 10^{-9} mbar. Large area lens mode was used for both wide and narrow scans. For the wide scan, the energy pass was 90 eV, the energy step was 0.5 eV and the scan number was 4. For the narrow high-resolution scans (N^{1s} and Au^{4f}) the energy pass was 50 eV, the energy step was 0.2 eV and the scan number was 20. The spectra were then analyzed using CasaXPS software. The variations in the polymer bond vibration induced by the incorporation of AuNRs were tracked by a Horiba John Yvon HR800 UV Raman Lab system coupled with a laser source of 635 nm wavelength to scan AuNRs, polymer and nanocomposite samples in the range of 100 to 1800 cm^{-1}. The conductivity of the polymer and nanocomposite films was measured by a Suss MicroTec PM5 probe station and Keithly 2612 semiconductor parameter analyzer system. Gold and silver ion concentrations were determined by Thermo Fisher Scientific Inductively coupled plasma (ICP, ICAP 6300 DUO) atomic emission spectrometer. In the photosensitivity experiments, CW 705 nm Red diode laser Thorlabs Fabry-Perot was employed as a light source to irradiate the nanocomposite film.

Results and Discussion

The morphology and optical properties of the AuNRs synthesized by the photochemical method are presented as supporting information. The UV-Vis absorption spectra of PANI/CSA-ES and PANI/CSA-ES-AuNRs nanocomposites are shown in **figure 1 (a)**. The characteristic peaks of PANI/CSA-ES at ~350 nm (3.58 eV) ~420 nm (2.95 eV) and ~800 nm (1.55 eV) attributed to π–π*, polaron-π* and π–polaron transitions, respectively, are all evident in the spectrum [55]. The shoulder at ~420 nm is usually assigned to the protonation of the polymer chains due to doping, and the generation of interband gap state associated with polaron production [55-59]. The embedding of AuNRs into PANI/CSA-ES significantly strengthens the intensity of the absorption peak at ~350 nm compared to the shoulder at ~420 nm, and redshifts the absorption of the π-polaron transition from ~800 nm (1.55 eV) to ~850 nm (1.45 eV). The increase of the absorption at 350 nm implies the augmentation of the π–π* transition through the interaction of the AuNRs with the polymer chains. The high wavelength polaron band, in the range of 750 to 850 nm, is usually related to a “compact coil” conformation of the polymer. Therefore, the redshift of this band may suggest an increase in the conjugation length of the polymer by uncoiling the polymer chains [37b]. Hence, the redshift of the π-polaron transition by incorporating the AuNRs with the PANI/CSA-ES from 800 to around 850 indicates the change in the stacking structure of the PANI chains within each other and increases the active conjugation length, resulting in a significant decline in the π-polaron band transition energy gap. This may be evidence of the intercalation of the AuNRs in between the PANI chains. It is important to notice that this redshift is unrelated neither to the aspect ratio nor the concentration of the NRs. The involved AuNRs interact with the PANI/CSA-ES polymer chains and boost the charge transfer transition by generating more polarons or lowering the π-polaron transition energy gap. The characteristic absorption

spectra of AuNRs (the Longitudinal and Transverse Surface Plasmon Resonance (LSPR), and (TSPR)) completely cover that of PANI giving rise to a small shoulder in the range between 570 and 710 with a hump at around 600 nm (appointed by black arrow) and possibly affecting the redshift of the absorption peak relevant to the π-polaronic band transition. The new humps around 600 nm may refer to the novel charge transfer transition between the AuNRs and the PANI/CSA-ES polymer chains as its position is irrelevant to the NR's aspect ratio.

Figure 1;

Figure 1 (b) depicts the FTIR spectra of PANI/CSA-ES and of PANI/CSA-ES/AuNR composites with AuNR aspect ratios 2.5 and 3.8 (composites V and IV, respectively). The bands observed for the PANI/CSA-ES emeraldine salt (ES) at 2367 and 1742 cm^{-1}, attributed to C=N-Ar and $C=NH^{+}$ stretching vibrations, and the band at 1594 cm^{-1}, assigned to the quinonoid ring stretching[60-63] do not change with the incorporation of AuNRs to the PANI/CA matrix. Similarly, the absorption peak at 824 cm^{-1} assigned to the aromatic C-H out-of-plane-bending on *p*-disubstituted ring, the vibration peaks at 786 – 791 cm^{-1} assigned to the stretching vibration of the p-disubstituted benzene ring (bending of C=C) and the vibrational peak at 1040 cm^{-1}, assigned to the O=S=O stretching mode of Camphor sulfonic acid[56], hold steady after the addition of AuNRs. Remarkably, the peak at 1167 cm^{-1}, assigned to the in-plane bending vibration mode of $C=NH^{+}$ in the quinonoid ring after incorporating the AuNRs, blue shifts to 1153 cm^{-1}. The blue shift of this band is usually attributed to electron delocalization in the PANI chain. Furthermore, the peak of doped PANI at 1507 cm^{-1}, assigned to the ring stretching vibration of benzenoid C=C, blue shifts to 1466 and 1475 cm^{-1} in case of nanocomposites IV and V, respectively. These results unambiguously indicate that the extent of the polaron delocalization in the nanocomposites is larger than that in PANI/CSA-ES, confirming the role of the AuNRs as secondary dopants in PANI.

Figure 2;

In **Figure 2**, the Raman measurements of PANI/CSA-ES and nanocomposite samples are reported. The characteristic vibrational peaks related to PANI in its different forms and after AuNRs hybridization are assigned in the graph. The vibrations of the C-H (quinonoid ring) increased in intensity both with CSA doping and AuNRs embedding, as results comparing the intensity of the peak at 1148 cm^{-1} with the vibrational peak at 1189 cm^{-1} [64]. The C-N stretching vibration peak, at 1229 cm^{-1} remarkably shifts after AuNRs incorporation to 1269 cm^{-1}, suggesting the tendency of AuNRs to interact with C-N bonds of PANI chains. The intensity of the vibrational peak at 1343 cm^{-1}, assigned to the $C\text{-}N^{\bullet+}$ radical cation band stretching, increased with both acid doping and NRs incorporation [65-68]. The peak at 1398 cm^{-1}, usually assigned to the free charge carrier vibration, shifts from 1404 for the doped form to 1416 cm^{-1} for the nanocomposite, suggesting enhancement of the delocalization[69]. Moreover, the stretching vibration of the quinonoid ring C=N bond, at 1470 cm^{-1}, shifts slightly in the nanocomposite to 1472 cm^{-1}. The incorporation of the AuNRs affect the vibrational mode of both the benzenoid and quinonoid ring in PANI polymer chains as indicated by the small shifts of the peaks at 1572, 1608, and 1642 cm^{-1}, assigned to C=C stretching of the quinonoid ring and C-C stretching of the benzene ring.

Figure 3;

Next, XPS characterization was performed on PANI Emeraldine Base (PANI-EB), PANI/CSA-ES and on the nanocomposite type IV samples. The deconvolution of N 1s core-level spectrum of PANI-EB leads to two major peaks

at 399.1 and 401.6 eV representing, respectively, the imine and amine groups, as shown in **Figure 3 (a)**. Upon acid doping, the imine band increases whereas the amine one decreases, and this relative change of intensities becomes more prominent in the case of the nanocomposite with added AuNRs. The enhanced change in the ratio between amine and imine bands in the nanocomposite might be attributed to the modification in the doping level of the PANI as aforementioned in the electronic absorption spectra. Furthermore, the slight red shift in the amine and imine peak positions, which was observed with both acid doping and NR incorporation, can be attributed to the attenuation of the electron-cloud richness at the N atoms. Similar positive shifts up to 1.2 eV have been reported for PANI decorated with the gold clusters. Finally, the Au 4*f* core-level spectrum peaks of the AuNRs in the composite did not show any significant variation compared to pure gold, since the strong metal core signal [70] is not expected to be significantly affected by possible charge transfer between the nanocomposite components.

Figure 4;

Figures 4 a-c, show the TEM micrographs of PANI/CSA-ES-AuNR nanocomposites with NRs of different aspect ratios, drop casted from their solutions directly on the TEM grids. The AuNRs are clearly homogeneously distributed in the PANI matrix without any aggregation regardless of their aspect ratio. Furthermore, it was observed that the AuNRs with a high aspect ratio used in the experiments has a smaller width than low aspect ratio AuNRs. According to previous reports, a CTAB bilayer coats the AuNRs' surface after their synthesis exhibiting a positive charge on the external surface [71]. The positively charged NRs may be intercalated between the negatively charged doped polymer chains by electrostatic interactions. Therefore, by mixing PANI/CSA-ES with positively charged AuNRs, the conformation structure of the polymer chains may change where the AuNRs lie onto the polymer chains or stand as a connecting bridge between two adjacent polymer chains, as schematically shown in the scheme of **Figure 4 (d)**. The latter possibility would increase the d-spacing between the polymer chains depending on the longitudinal axis length of the NRs. Accordingly, the electric delocalized charges would transport between PANI chains through NR bridges as well as by hopping. When the NRs lie onto the polymer chains, they most likely facilitate the charge transport across the PANI chains.

In order to investigate the role of AuNRs on the nanocomposites' electrical conductivity, the concentration and the aspect ratio of the AuNRs were changed independently and the electrical conductivity was measured. At a stable AuNRs molar concentration of 65 nM, the electrical conductivity of the nanocomposites decreased with increasing aspect ratio, as shown in **Figure 5 (a)**. It should be noted here that for stable molar concentration, the atomic gold concentration [Au] decreases with increasing aspect ratio due to the decrease in the volume of a single nanorod. Consequently, the role of the [Au] concentration and NRs aspect ratio were evaluated separately, and it was found that at a stable [Au] concentration, the electrical conductivity of the nanocomposites increased by 14% with increasing aspect ratio by 51% from 2.9 to 3.8, **Figure 5 (b)**. This can be assigned to the increase of the effective contact surface area between the AuNRs and PANI chains with increasing the aspect ratio of the NRs, inducing enhancement of the charges mobility (or enhancement of the probability of charge transfer) between PANI chains and AuNRs. However, at a constant embedded nanorod aspect ratio in the nanocomposites, a considerable rise in the electrical conductivity of around 32% was measured by increasing the [Au] concentration from 65 to 87 nM, **Figure 5 (c)**. The decrease of [Au] concentration would be expected to reduce the rate of the charge transfer between AuNRs and PANI chains (decreasing the degree of metallization of the nanocomposite). Therefore, the electrical properties of the nanocomposites depend primarily on the amount of [Au] embedded in the polymer and secondly on the aspect ratio of the embedded AuNRs.

Figure 5;

It was proposed that when gold nanoparticles are introduced into the PANI matrix alongside an adequate electric field, charge transfer may be induced between PANI and gold nanoparticles through electron transfer from the imine nitrogen sites of the polymeric chains to the gold nanoparticles [72]. Therefore, gold nanoparticles act as a dopant, inducing the formation of additional polarons, and therefore leading to charge carrier density increase. The charge transfer efficiency was shown to be affected by the charge donating ability of the conjugated polymer PANI, the nanoparticles, size [58, 59, 70] and concentration [73], as well as the nature of the interface between gold nanoparticles and PANI. Furthermore, the presence of gold nanoparticle connections between the polymeric chains provides additional conductive pathways, reducing the trapping centers due to the heterogeneous nature of the polymer crystallographic domains. In our system, where the spherical gold nanoparticles were replaced by AuNRs, their elongated morphology is expected to further influence the charge mobility between PANI and AuNRs. As mentioned above, the positive charge of the NRs surface facilitates electron transfer between imine nitrogen sites of PANI and AuNRs. The charge transfer between AuNRs and imine nitrogens of polymer chains through a tunneling process is schematically shown in **Scheme 1**. That process may be induced by the electric field leading to a charge density increase. The increase of the charge density is enhanced not only by increasing the gold concentration but also by increasing the AuNRs aspect ratio, through the increase of the interfacial surface area with PANI chains.

Scheme 1;

Light sensing application

The selective sensitivity of the PANI/CSA-ES/AuNRs nanocomposites of specific light wavelength was investigated as an application. AuNRs with an aspect ratio of 2.5 and 3.8, corresponding to LSPR absorption peak maximums at 650 and 732 nm, ($AuNRs^{650}$, and $AuNRs^{732}$), respectively, were used to prepare the nanocomposites by mixing the same [Au] concentration with PANI/CSA-ES solutions. The photosensitivity of the nanocomposites was explored by measuring the variation of the current density across the nanocomposite films at different irradiances at the wavelength of 705 nm. **Figure 6 (a)** shows the relationship between the current density that passes through the nanocomposites and the incident light intensity at a constant applied voltage of 1 V, while **Figure 6 (b)** depicts the absorption spectra of the AuNRs used for the preparation of the nanocomposites, (the blue arrow indicates the laser wavelength used in the experiment). The variation of the current density was measured under irradiation of the nanocomposite films within a range of 0 to 150 mW/cm^2, and with steps of 10 mW/cm^2. Compared to the nanocomposites containing $AuNRs^{650}$(Comp V), the nanocomposites containing $AuNRs^{732}$ (Comp IV) show higher values of current density upon irradiation with 705 nm. The measured current density of Comp IV increased linearly with increasing irradiance from 30 to 130 mW/cm^2. The sensitivity of the Comp IV, estimated from the slope of the current density versus irradiance curve, is 6.2×10^{-4} $\mu A.\mu m^{-2}.mW^{-1}$. On the other hand, the nanocomposites containing $AuNRs^{650}$ (Comp V) did not exhibit any current density alteration, even at high irradiances. The incorporation of the $AuNRs^{650}$ with PANI/CSA-ES neither accelerates the mobility of the charge carriers nor generates new charge carriers under the irradiation conditions. Where the wavelength of the irradiation beam is far from exciting the LSP conduction electrons, as the maximum absorption of the LSPR is shorter by around 50 nm. The sensitivity of Comp IV to 705 nm light may originate from the excitation of the conduction electrons of the AuNRs with a laser beam when its wavelength is close to the maximum of the LSPR of the NRs (**Figure 6 (b)**), which appeared as an increment in the current density

with increasing irradiance. Therefore, the enhancement of the nanocomposite conductivity upon irradiation could be assigned to the excitation of the AuNR's LSPR, thereby increasing the charge mobility between AuNRs and PANI.

Figure 6;

Next, the response time of the system of PANI/CSA-ES-AuNRs^{732} nanocomposite films upon irradiation at 705 nm was investigated to understand the dynamics of the system and reproducibility of the photosensitivity. The changes in the current density of the Comp IV film versus time upon on/off NIR irradiation cycles, at an irradiance of 100 mW/cm^2 and an applied voltage of 1 V, are shown in **Figure 7 (a)**. The reversibility of the photoresponse of the tested films was confirmed repeating 7 cycles of irradiation/dark every 30 seconds. The irradiation intervals are highlighted in red and the dark intervals in black. As shown in **Figure 7 (b)**, no enhancement of the current density was recorded on the PANI/CSA-ES polymer film without NRs, implying insensitivity of the pure doped PANI under the experimental conditions. The acid doping of the PANI generates charge carriers that are responsible for the electrical conductivity. Even with the high absorption of the PANI/CSA-ES film at the range from 700 to 80 nm, the irradiation with a laser beam of 705 nm light wavelength appears to be ineffective in boosting the current density by accelerating the existed charge carriers or creating new ones. It is clear that irradiation of the PANI/CSA-ES and Comp V films with 705 nm light did not exhibit any change in the passed current density, while the Comp IV containing AuNRs^{732} show a pertinent response. This reveals the importance of the AuNRs and the role of LSPR excitation with an appropriate light beam in the enhancement of the photosensitivity of the nanocomposite films.

The current density response curve to irradiation and dark recovery, depicted in **Figures 7 (c) and (d)**, is fitted by equation (1) [74, 75].

$$J = J_2 + (J_1 - J_2) / (1 + \exp((t - t_0) / dt)) \quad (1)$$

Where J_1 and J_2 are the initial and final current density values, respectively, while t_0 and dt represent the time of the central point of the current inflection and the time interval of significant current density change. After starting and suspending the NIR irradiation, the current density takes about 5.0 and 3.5 s to rise and fall, respectively. The rate of current density fall ($\approx 8.5 \times 10^{-8}$ $\mu A.\mu m^{-2}.s^{-1}$) is higher than that of the rise ($\approx 5.8 \times 10^{-8}$ $\mu A.\mu m^{-2}.s^{-1}$). This result sheds light on the kinetics of the charge carriers' separation and recombination as they are the main electronic processes stimulated by NIR irradiation. Since the selected wavelength of irradiation, 705 nm, is close to the LSPR maximum absorption ($\approx$ 732 nm) of the AuNRs used, the irradiation causes AuNRs stimulation, affecting the electron dynamics (electron-electron and electron-phonon scattering) in the conduction band [44]. Irradiation of the AuNRs leads to surface plasmon coherent electronic oscillation as well as enhancement of the d-*sp* interband electronic transition [76]. The electrons excited to the sp-orbital and the holes in the d-band of the NRs can be redistributed at the interface between AuNRs and PANI. The excited charge transfer reduces the recombination of the electrons and holes in both PANI and AuNRs. Therefore, the excited charges of AuNRs transfer by hopping to PANI chains, increasing the charge density over the nanocomposite lattice. By suspending the irradiation, the excited electrons collapse and fall down to the d orbital, leading to recombination of charge carriers. The presence of charge trapping centers on the polymer chains might be responsible for the delay of the response to irradiation's variation with respect to the current drop. These charge trapping centers result from the morphologically complex nature of PANI, which consists of amorphous regions among the crystalline domains [77-83].

Figure 7;

The role of the AuNRs on the overall photosensitivity of the nanocomposites was further studied by measuring the maximum charge generation rate (G_{max}) [74, 75]. The complete calculation and the experiment conditions are represented as supporting information. The results showed that the G_{max} of the PANI/CSA-ES is unaffected by the irradiating light wavelength. However, in the case of the nanocomposites, the G_{max} is enhanced for irradiation close to the NRs plasmonic maximum absorption. This gives an insight into the plasmonic excitation of the embedded NRs and its impact on the enhancement of the charge transfer between the PANI and the AuNRs.

Further studies on the roles of the PANI oxidation states, the doping degree, and the surface chemistry of the AuNRs are important to fully understand the nature of the charge transfer between the AuNRs and the PANI chains. This could lead to an optoelectronic device with selective characters.

Conclusions

PANI-AuNRs nanocomposites were prepared by mixing different aspect ratio AuNRs with PANI/CSA-ES. The NRs were homogeneously dispersed in the PANI/CSA-ES matrix, reflecting a good affinity between the capping molecules of the NRs and the polymer matrix. The addition of NRs, independent from the aspect ratio, has an impact on the electronic transitions of the nanocomposite. Both of the π-π^* and polaronic band-π^* transitions were enhanced by AuNR incorporation, as the absorption spectra reveal. FTIR and micro Raman spectra manifested, that the mingling of AuNRs with PANI/CSA-ES induced the extension of the electronic delocalization across the polymer due to the affinity of the NRs to the nitrogen atoms of the polymer backbone. The incorporation of the NRs boosts the nanocomposites' electrical conductivity of about one order of magnitude. The nanocomposite's conductivity was increased both by increasing the atomic gold concentration and the NR's aspect ratio. The increase of the NR's surface at the larger aspect ratios lead to the enhancement of the interaction between the NRs and polymer chains through expanding the interfacial contact area, facilitating the charge transition between the polymer and the NRs. The selective photodetection of the nanocomposites was also examined. Irradiation of the nanocomposites at a wavelength near the wavelength of their longitudinal plasmonic resonance induces the delocalization of the NRs surface plasmonic electrons. The interaction between the excited surface plasmon and PANI accelerates the charge transition between PANI and the NRs and reduces the charge recombination. The result is an increased current density when the nanocomposites were irradiated at a wavelength that coincides with the longitudinal plasmonic resonance absorption of the incorporated nanorods.

References:

[1] Mirmohseni A, Oladegaragoze A. Anti-corrosive properties of polyaniline coating on iron. Synthetic Metals. 2000;114(2):105-8.
[2] Yang JP, Rannou P, Planès J, Proń A, Nechtschein M. Preparation of low density polyethylene-based polyaniline conducting polymer composites with low percolation threshold via extrusion. Synthetic Metals. 1998;93(3):169-73.
[3] Cao Y, Smith P, Heeger AJ. Counter-ion induced processibility of conducting polyaniline. Synthetic Metals. 1993;57(1):3514-9.
[4] Laska J, Zak K, Proń A. Conducting blends of polyaniline with conventional polymers. Synthetic Metals. 1997;84(1):117-8.
[5] Zilberman M, Titelman GI, Siegmann A, Haba Y, Narkis M, Alperstein D. Conductive blends of thermally dodecylbenzene sulfonic acid-doped polyaniline with thermoplastic polymers. Journal of Applied Polymer Science. 1997;66(2):243-53.
[6] Lira LM, Córdoba de Torresi SI. Conducting polymer–hydrogel composites for electrochemical release devices: Synthesis and characterization of semi-interpenetrating polyaniline–polyacrylamide networks. Electrochemistry Communications. 2005;7(7):717-23.
[7] Garjonyte R, Malinauskas A. Amperometric glucose biosensors based on Prussian Blue– and polyaniline–glucose oxidase modified electrodes. Biosensors and Bioelectronics. 2000;15(9–10):445-51.
[8] Karyakin AA, Vuki M, Lukachova LV, Karyakina EE, Orlov AV, Karpachova GP, et al. PROCESSIBLE POLYANILINE AS AN ADVANCED POTENTIOMETRIC pH TRANSDUCER. APPLICATION TO BIOSENSORS. Analytical Chemistry. 1999;71(13):2534-40.
[9] Ma Y, Ali SR, Dodoo AS, He H. Enhanced Sensitivity for Biosensors: Multiple Functions of DNA-Wrapped Single-Walled Carbon Nanotubes in Self-Doped Polyaniline Nanocomposites. The Journal of Physical Chemistry B. 2006;110(33):16359-65.
[10] Campos TLA, Kersting DF, Ferreira CA. Chemical synthesis of polyaniline using sulphanilic acid as dopant agent into the reactional medium. Surface and Coatings Technology. 1999;122(1):3-5.
[11] Bhadra S, Singha NK, Khastgir D. Electrochemical synthesis of polyaniline and its comparison with chemically synthesized polyaniline. Journal of Applied Polymer Science. 2007;104(3):1900-4.
[12] Duić L, Mandić Z. Counter-ion and pH effect on the electrochemical synthesis of polyaniline. Journal of Electroanalytical Chemistry. 1992;335(1):207-21.
[13] Zahn DRT, Gavrila GN, Salvan G. Electronic, and Vibrational Spectroscopies Applied to Organic/Inorganic Interfaces. Chemical Reviews. 2007;107(4):1161-232.
[14] Baibarac M, Baltog I, Lefrant S, Mevellec JY, Chauvet O. Polyaniline and Carbon Nanotubes Based Composites Containing Whole Units and Fragments of Nanotubes. Chemistry of Materials. 2003;15(21):4149-56.
[15] Philip B, Xie J, Abraham JK, Varadan VK. Polyaniline/carbon nanotube composites: starting with phenylamino functionalized carbon nanotubes. Polymer Bulletin. 2005;53(2):127-38.
[16] Salvatierra RV, Cava CE, Roman LS, Zarbin AJG. ITO-Free and Flexible Organic Photovoltaic Device Based on High Transparent and Conductive Polyaniline/Carbon Nanotube Thin Films. Advanced Functional Materials. 2013;23(12):1490-9.
[17] Xia H, Wang Q. Ultrasonic Irradiation: A Novel Approach To Prepare Conductive Polyaniline/Nanocrystalline Titanium Oxide Composites. Chemistry of Materials. 2002;14(5):2158-65.
[18] Su S-J, Kuramoto N. Processable polyaniline–titanium dioxide nanocomposites: effect of titanium dioxide on the conductivity. Synthetic Metals. 2000;114(2):147-53.
[19] Qiao Y, Bao S-J, Li CM, Cui X-Q, Lu Z-S, Guo J. Nanostructured Polyaniline/Titanium Dioxide Composite Anode for Microbial Fuel Cells. ACS Nano. 2008;2(1):113-9.
[20] Yoneyama H, Tokuda M, Kuwabata S. Photo-induced electrochromic reactions of deprotonated polyaniline containing cadmium sulfide particles. Electrochimica Acta. 1994;39(8):1315-20.
[21] Chandrakanthi RLN, Careem MA. Preparation and characterization of CdS and Cu2S nanoparticle/polyaniline composite films. Thin Solid Films. 2002;417(1–2):51-6.
[22] Dhanabalan A, Talwar SS, Contractor AQ, Kumar NP, Narang SN, Major SS, et al. Polyaniline–CdS Composite Films Obtained from Polyaniline–Cadmium Arachidate Multilayers. Journal of Materials Science Letters. 1999;18(8):603-6.
[23] Khiew PS, Huang NM, Radiman S, Ahmad MS. Synthesis, and characterization of conducting polyaniline-coated cadmium sulphide nanocomposites in reverse microemulsion. Materials Letters. 2004;58(3–4):516-21.
[24] Tseng RJ, Huang J, Ouyang J, Kaner RB, Yang. Polyaniline Nanofiber/Gold Nanoparticle Nonvolatile Memory. Nano Letters. 2005;5(6):1077-80.
[25] Del Castillo-Castro T, Larios-Rodriguez E, Molina-Arenas Z, Castillo-Ortega MM, Tanori J. Synthesis and characterization of metallic nanoparticles and their incorporation into electroconductive polymer composites. Composites Part A: Applied Science and Manufacturing. 2007;38(1):107-13.
[26] Peng Z, Guo L, Zhang Z, Tesche B, Wilke T, Ogermann D, et al. Micelle-Assisted One-Pot Synthesis of Water-Soluble Polyaniline−Gold Composite Particles. Langmuir. 2006;22(26):10915-8.
[27] Kumar NA, Choi H-J, Shin YR, Chang DW, Dai L, Baek J-B. Polyaniline-Grafted Reduced Graphene Oxide for Efficient Electrochemical Supercapacitors. ACS Nano. 2012;6(2):1715-23.

[28] Tian S, Liu J, Zhu T, Knoll W. Polyaniline/Gold Nanoparticle Multilayer Films: Assembly, Properties, and Biological Applications. Chemistry of Materials. 2004;16(21):4103-8.
[29] Baker CO, Shedd B, Tseng RJ, Martinez-Morales AA, Ozkan CS, Ozkan M, et al. Size Control of Gold Nanoparticles Grown on Polyaniline Nanofibers for Bistable Memory Devices. ACS Nano. 2011;5(5):3469-74.
[30] Nirmala Grace A, Pandian K. Pt, Pt–Pd and Pt–Pd/Ru nanoparticles entrapped polyaniline electrodes – A potent electrocatalyst towards the oxidation of glycerol. Electrochemistry Communications. 2006;8(8):1340-8.
[31] Gao Y, Shan D, Cao F, Gong J, Li X, Ma H-y, et al. Silver/Polyaniline Composite Nanotubes: One-Step Synthesis and Electrocatalytic Activity for Neurotransmitter Dopamine. The Journal of Physical Chemistry C. 2009;113(34):15175-81.
[32] Ma Y, Li N, Yang C, Yang X. One-step synthesis of water-soluble gold nanoparticles/polyaniline composite and its application in glucose sensing. Colloids and Surfaces A: Physicochemical and Engineering Aspects. 2005;269(1–3):1-6.
[33] Hu Z-A, Xie Y-L, Wang Y-X, Mo L-P, Yang Y-Y, Zhang Z-Y. Polyaniline/SnO2 nanocomposite for supercapacitor applications. Materials Chemistry and Physics. 2009;114(2–3):990-5.
[34] Nesher G, Aylien M, Sandaki G, Avnir D, Marom G. Polyaniline Entrapped in Silver: Structural Properties and Electrical Conductivity. Advanced Functional Materials. 2009;19(8):1293-8.
[35] Santos RFS, Andrade CAS, dos Santos CG, de Melo CP. Visible luminescence in polyaniline/(gold nanoparticle) composites. Journal of Nanoparticle Research. 2013;15(1):1408.
[36] Saheb AH, Seo SS. UV-Vis and Raman Spectral Analysis of Polyaniline/Gold Thin Films as a Function of Applied Potential. Analytical Letters. 2011;44(7):1206-16.
[37] Afzal AB, Akhtar MJ, Nadeem M, Hassan MM. Investigation of Structural and Electrical Properties of Polyaniline/Gold Nanocomposites. The Journal of Physical Chemistry C. 2009;113(40):17560-5.
[38] Yang W, Liu J, Zheng R, Liu Z, Dai Y, Chen G, et al. Ionic Liquid-assisted Synthesis of Polyaniline/Gold Nanocomposite and Its Biocatalytic Application. Nanoscale Research Letters. 2008;3(11):468.
[39] Tanami G, Gutkin V, Mandler D. Thin Nanocomposite Films of Polyaniline/Au Nanoparticles by the Langmuir−Blodgett Technique. Langmuir. 2010;26(6):4239-45.
[40] Li X, Chen W, Bian C, He J, Xu N, Xue G. Surface modification of TiO2 nanoparticles by polyaniline. Applied Surface Science. 2003;217(1–4):16-22.
[41] O'Mullane AP, Dale SE, Macpherson JV, Unwin PR. Fabrication and electrocatalytic properties of polyaniline/Pt nanoparticle composites. Chemical Communications. 2004(14):1606-7.
[42] Xian Y, Hu Y, Liu F, Xian Y, Wang H, Jin L. Glucose biosensor based on Au nanoparticles–conductive polyaniline nanocomposite. Biosensors and Bioelectronics. 2006;21(10):1996-2000.
[43] Braun S, Salaneck WR, Fahlman M. Energy-Level Alignment at Organic/Metal and Organic/Organic Interfaces. Advanced Materials. 2009;21(14-15):1450-72.
[44] Link S, El-Sayed MA. Spectral Properties and Relaxation Dynamics of Surface Plasmon Electronic Oscillations in Gold and Silver Nanodots and Nanorods. The Journal of Physical Chemistry B. 1999;103(40):8410-26.
[45] Link S, El-Sayed MA. Shape and size dependence of radiative, non-radiative and photothermal properties of gold nanocrystals. International Reviews in Physical Chemistry. 2000;19(3):409-53.
[46] Jain PK, Lee KS, El-Sayed IH, El-Sayed MA. Calculated Absorption and Scattering Properties of Gold Nanoparticles of Different Size, Shape, and Composition: Applications in Biological Imaging and Biomedicine. The Journal of Physical Chemistry B. 2006;110(14):7238-48.
[47] Obare SO, Jana NR, Murphy CJ. Preparation of Polystyrene- and Silica-Coated Gold Nanorods and Their Use as Templates for the Synthesis of Hollow Nanotubes. Nano Letters. 2001;1(11):601-3.
[48] Wijaya A, Hamad-Schifferli K. Ligand Customization and DNA Functionalization of Gold Nanorods via Round-Trip Phase Transfer Ligand Exchange. Langmuir. 2008;24(18):9966-9.
[49] Link S, Mohamed MB, El-Sayed MA. Simulation of the Optical Absorption Spectra of Gold Nanorods as a Function of Their Aspect Ratio and the Effect of the Medium Dielectric Constant. The Journal of Physical Chemistry B. 1999;103(16):3073-7.
[50] Lee K-S, El-Sayed MA. Dependence of the Enhanced Optical Scattering Efficiency Relative to That of Absorption for Gold Metal Nanorods on Aspect Ratio, Size, End-Cap Shape, and Medium Refractive Index. The Journal of Physical Chemistry B. 2005;109(43):20331-8.
[51] Abdelrasoul GN, Scotto M, Cingolani R, Diaspro A, Athanassiou A, Pignatelli F. Effect of precursor solution dark incubation on gold nanorods morphology. Journal of Crystal Growth. 2012;361:159-65.
[52] Kim F, Song JH, Yang P. Photochemical Synthesis of Gold Nanorods. Journal of the American Chemical Society. 2002;124(48):14316-7.
[53] Abdelrasoul GN, Cingolani R, Diaspro A, Athanassiou A, Pignatelli F. Photochemical synthesis: Effect of UV irradiation on gold nanorods morphology. Journal of Photochemistry and Photobiology A: Chemistry. 2014;275:7-11.
[54] Niidome Y, Nishioka K, Kawasaki H, Yamada S. Rapid synthesis of gold nanorods by the combination of chemical reduction and photoirradiation processes; morphological changes depending on the growing processes. Chemical Communications. 2003(18):2376-7.

[55] Xia Y, Wiesinger JM, MacDiarmid AG, Epstein AJ. Camphorsulfonic Acid Fully Doped Polyaniline Emeraldine Salt: Conformations in Different Solvents Studied by an Ultraviolet/Visible/Near-Infrared Spectroscopic Method. Chemistry of Materials. 1995;7(3):443-5.
[56] Arenas MC, Sánchez G, Nicho ME, Elizalde-Torres J, Castaño VM. Engineered doped and codoped polyaniline gas sensors synthesized in N,N,dimethylformamide media. Applied Physics A. 2012;106(4):901-8.
[57] He C, Tan Y, Li Y. Conducting polyaniline nanofiber networks prepared by the doping induction of camphor sulfonic acid. Journal of Applied Polymer Science. 2003;87(9):1537-40.
[58] Mallick K, Witcomb MJ, Scurrell MS. Gold in polyaniline: Recent trends. Gold Bulletin. 2006;39(4):166-74.
[59] Boonchu C, Kane-Maguire LAP, Wallace GG. The Effect of Added Water on the Conformation of Optically Active Polyaniline in Organic Solvents. Synthetic Metals. 2003;135–136:241-2.
[60] Tang J, Jing X, Wang B, Wang F. Infrared spectra of soluble polyaniline. Synthetic Metals. 1988;24(3):231-8.
[61] Amarnath CA, Palaniappan S. Polyaniline doped by a new class of dopants, benzoic acid and substituted benzoic acid: synthesis and characterization. Polymers for Advanced Technologies. 2005;16(5):420-4.
[62] Hatchett DW, Josowicz M, Janata J. Acid Doping of Polyaniline: Spectroscopic and Electrochemical Studies. The Journal of Physical Chemistry B. 1999;103(50):10992-8.
[63] Bober P, Trchová M, Prokeš J, Varga M, Stejskal J. Polyaniline–silver composites prepared by the oxidation of aniline with silver nitrate in solutions of sulfonic acids. Electrochimica Acta. 2011;56(10):3580-5.
[64] Šeděnková I, Trchová M, Stejskal J, Prokeš J. Solid-State Reduction of Silver Nitrate with Polyaniline Base Leading to Conducting Materials. ACS Applied Materials & Interfaces. 2009;1(9):1906-12.
[65] Izumi CMS, Andrade GFS, Temperini MLA. Surface-Enhanced Resonance Raman Scattering of Polyaniline on Silver and Gold Colloids. The Journal of Physical Chemistry B. 2008;112(51):16334-40.
[66] Šeděnková I, Trchová M, Stejskal J. Thermal degradation of polyaniline films prepared in solutions of strong and weak acids and in water – FTIR and Raman spectroscopic studies. Polymer Degradation and Stability. 2008;93(12):2147-57.
[67] do Nascimento GM, Temperini MrLA. Studies on the resonance Raman spectra of polyaniline obtained with near-IR excitation. Journal of Raman Spectroscopy. 2008;39(7):772-8.
[68] Lindfors T, Ivaska A. Raman based pH measurements with polyaniline. Journal of Electroanalytical Chemistry. 2005;580(2):320-9.
[69] da Silva JEP, de Torresi SIC, de Faria DLA, Temperini MLA. Raman characterization of polyaniline induced conformational changes. Synthetic Metals. 1999;101(1):834-5.
[70] Shukla S, Seal S. Cluster size effect observed for gold nanoparticles synthesized by sol-gel technique as studied by X-ray photoelectron spectroscopy. Nanostructured Materials. 1999;11(8):1181-93.
[71] Nikoobakht B, El-Sayed MA. Evidence for Bilayer Assembly of Cationic Surfactants on the Surface of Gold Nanorods. Langmuir. 2001;17(20):6368-74.
[72] Tseng RJ, Baker CO, Shedd B, Huang J, Kaner RB, Ouyang J, et al. Charge transfer effect in the polyaniline-gold nanoparticle memory system. Applied Physics Letters. 2007;90(5):053101.
[73] Sanches EA, Soares JC, Iost RM, Marangoni VS, Trovati G, Batista T, et al. Structural characterization of emeraldine-salt polyaniline/gold nanoparticles complexes. J Nanomaterials. 2011;2011:73-.
[74] Wu J-L, Chen F-C, Hsiao Y-S, Chien F-C, Chen P, Kuo C-H, et al. Surface Plasmonic Effects of Metallic Nanoparticles on the Performance of Polymer Bulk Heterojunction Solar Cells. ACS Nano. 2011;5(2):959-67.
[75] Lu L, Luo Z, Xu T, Yu L. Cooperative Plasmonic Effect of Ag and Au Nanoparticles on Enhancing Performance of Polymer Solar Cells. Nano Letters. 2013;13(1):59-64.
[76] Mohamed MB, Volkov V, Link S, El-Sayed MA. The `lightning' gold nanorods: fluorescence enhancement of over a million compared to the gold metal. Chemical Physics Letters. 2000;317(6):517-23.
[77] Annapoorni S, Sundaresan NS, Pandey SS, Malhotra BD. Photocarrier mobility in processable polyaniline. Journal of Applied Physics. 1993;74(3):2109-11.
[78] Bondarenko VE, Zhuravleva TS, Efimov ON, Nikolaeva GV. Delay photoconductivity in polyaniline films from different solvents. Synthetic Metals. 1997;84(1):793-4.
[79] Bondarenko VE, Zhuravleva TS, Efimov ON, Nikolaeva GV. Pulsed photoconductivity in composite polyaniline-polyvinyl alcohol films. Synthetic Metals. 1999;102(1):1228-9.
[80] Zhuravleva TS, Gladkevich AV, Misurkin PI. Delay photoconductivity of emeraldine base films. Synthetic Metals. 1995;69(1):269-70.
[81] Phillips SD, Yu G, Cao Y, Heeger AJ. Spectroscopy and transient photoconductivity of partially crystalline polyaniline. Physical Review B. 1989;39(15):10702-7.
[82] Stafström S, Brédas JL, Epstein AJ, Woo HS, Tanner DB, Huang WS, et al. Polaron lattice in highly conducting polyaniline: Theoretical and optical studies. Physical Review Letters. 1987;59(13):1464-7.
[83] Barazzouk S, Kamat PV, Hotchandani S. Photoinduced Electron Transfer between Chlorophyll a and Gold Nanoparticles. The Journal of Physical Chemistry B. 2005;109(2):716-23.

Figure Captions

Figure 1; Normalized spectroscopic characterization of PANI and nanocomposite solutions: (a) UV-Vis absorption spectra of PANI/CSA-ES and PANI/CSA-ES/AuNRs nanocomposites with different NR aspect ratios 2.5 (Comp I), 2.9 (Comp II) and 3.8 (Comp IV) and loadings (pH = 4 for all solutions) and (b) FT-IR spectra of PANI/CSA-ES and two nanocomposites with 2.5 (Comp V) and 3.8 (Comp IV) AuNRs aspect ratios.

Figure 2; Raman spectra of the PANI Emeraldine base, acid salt, and PANI/CSA-ES/AuNRs Comp IV.

Figure 3; XPS spectra of Polyaniline-Au nanorods, (a) N (1s) deconvoluted spectra of PANI-EB, (b) N (1s) deconvoluted spectra of PANI-ES, (c) N (1s) deconvoluted spectra of PANI-ES/AuNRs composites, (d) the core level spectra of Au 4f in AuNRs incorporated with PANI-ES.

Figure 4; TEM images of, (a) Comp. I, (b) Comp. II, and (c) Comp. III. The scale bar is 100 nm for all images. (d) Proposed arrangement of AuNRs and PANI chains.

Figure 5; Conductivity measurements of PANI/CSA-ES and PANI/CSA-ES-AuNRs nanocomposites: (a) Effect of AuNR aspect ratio and atomic gold concentration [Au] on the electrical conductivity, (b) effect of AuNRs aspect ratio at constant [Au] on the electrical conductivity, and (c) the effect of the atomic gold concentration [Au] on the electrical conductivity of the resulting nanocomposites for the same aspect ratio.

Scheme 1; Charge transfer processes between imine nitrogen of PANI and AuNRs.

Figure 6; (a) Photosensitivity of the PANI/CSA-ES-AuNRs nanocomposites at an applied voltage of 1 V. Red triangles and black squares refer respectively to measurements on Comp IV with embedded $AuNRs^{732}$, and on Comp I, with embedded $AuNRs^{650}$. (b) The absorption spectra of the AuNRs aqueous dispersions, where the blue arrow indicate the wavelength of the laser that was used during the experiment.

Figure 7; Conductivity response of (a) PANI/CSA-ES-AuNRs (AuNRs of LSP 732 nm) (Comp IV) nanocomposite film and (b) PANI/CSA-ES film toward fluctuated NIR irradiation (λ = 705 nm, light irradiance: 100 mW/cm^2) at an applied voltage of 1 V. The upward and downward transitions of the third conductivity response cycle are zoomed in (c) and (d), respectively, accompanied with the sigmoidal fitting (the solid line).

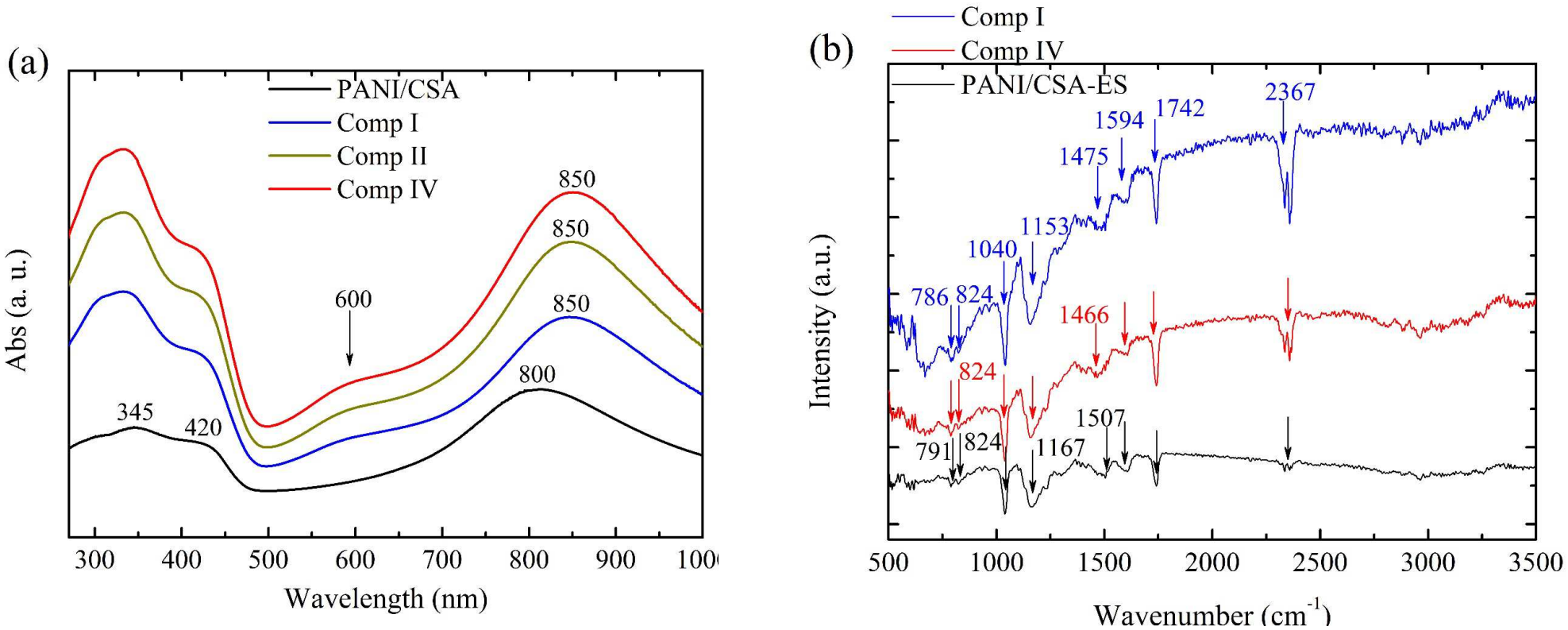
(a)
PANI/CSA
Comp I
Comp II
Comp IV
Abs (a. u.)
Wavelength (nm)
345
420
600
800
850
850
850
300
400
500
600
700
800
900
(b)
Comp I
Comp IV
PANI/CSA-ES
Intensity (a.u.)
Wavenumber (cm-1)
786
824
1040
1153
1475
1594
1742
2367
824
1466
791
824
1167
1507
500
1000
1500
2000
2500
3000
3500

Figure 1

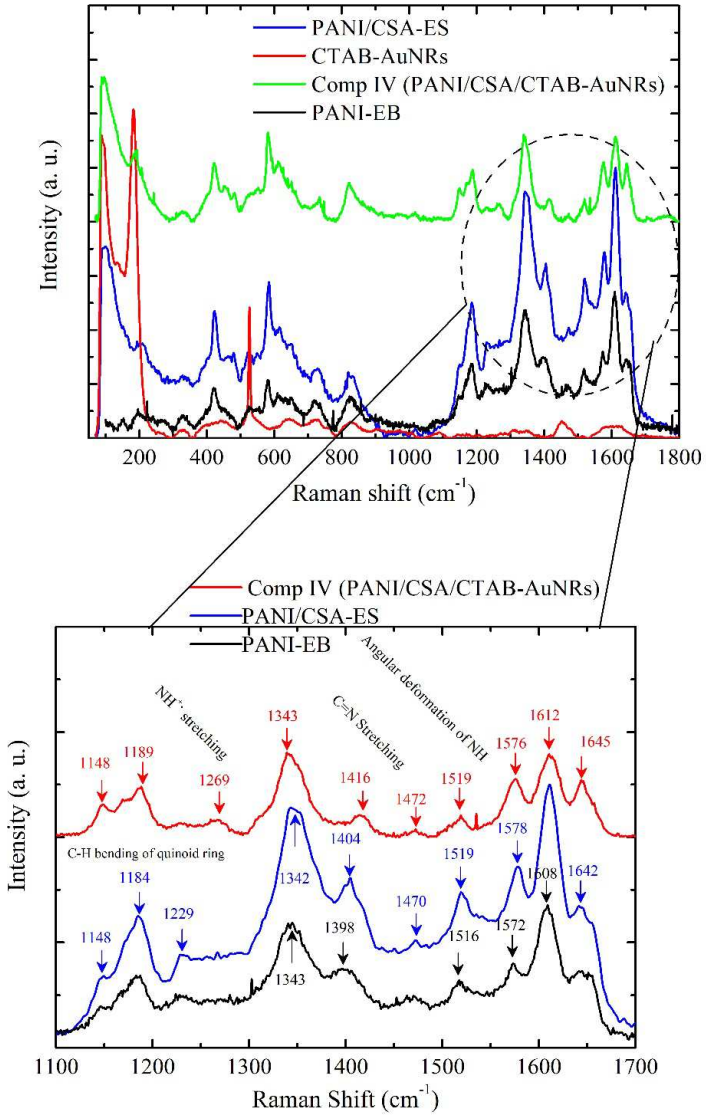
PANI/CSA-ES
CTAB-AuNRs
Comp IV (PANI/CSA/CTAB-AuNRs)
PANI-EB
Intensity (a. u.)
200 400 600 800 1000 1200 1400 1600 1800
Raman shift (cm-1)
Comp IV (PANI/CSA/CTAB-AuNRs)
PANI/CSA-ES
PANI-EB
NH+ stretching
C=N Stretching
Angular deformation of NH
1148
1189
1269
1343
1416
1472
1519
1576
1612
1645
C-H bending of quinoid ring
1148
1184
1229
1342
1404
1470
1516
1578
1608
1642
1343
1398
1572
Intensity (a. u.)
1100 1200 1300 1400 1500 1600 1700
Raman Shift (cm-1)

Figure 2

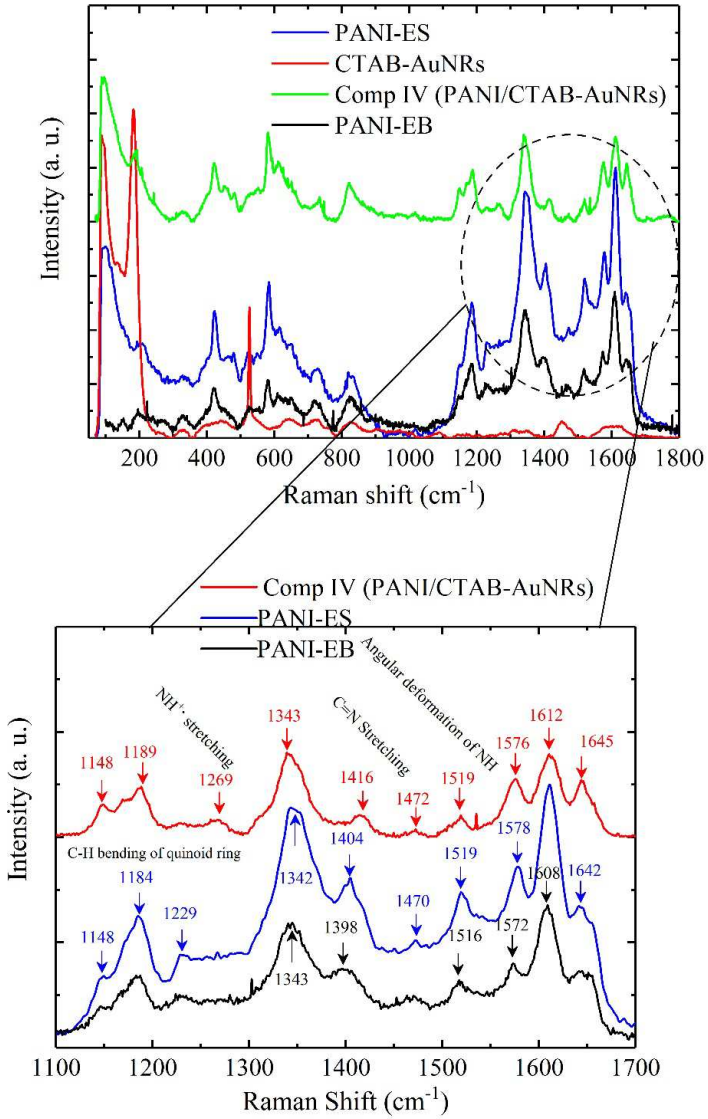

Figure 2

Enhanced resolution

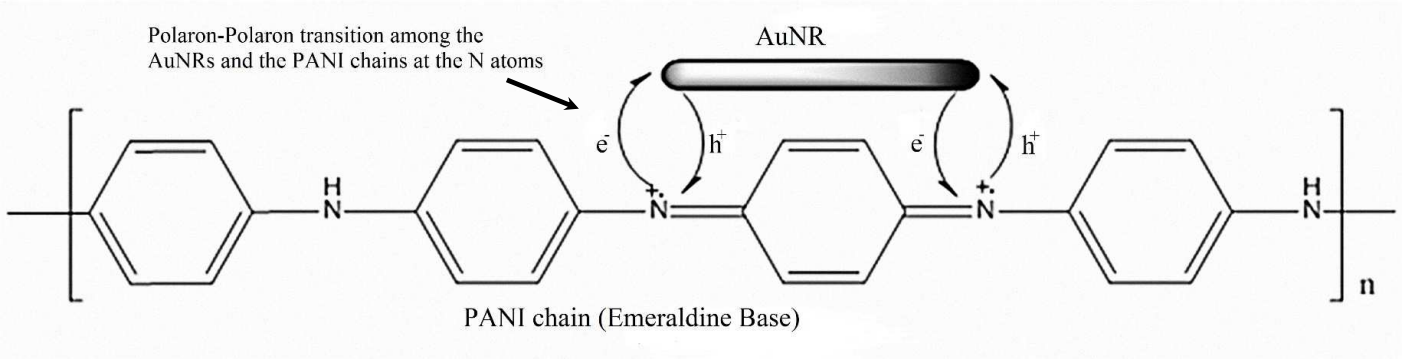

Scheme 1

modified

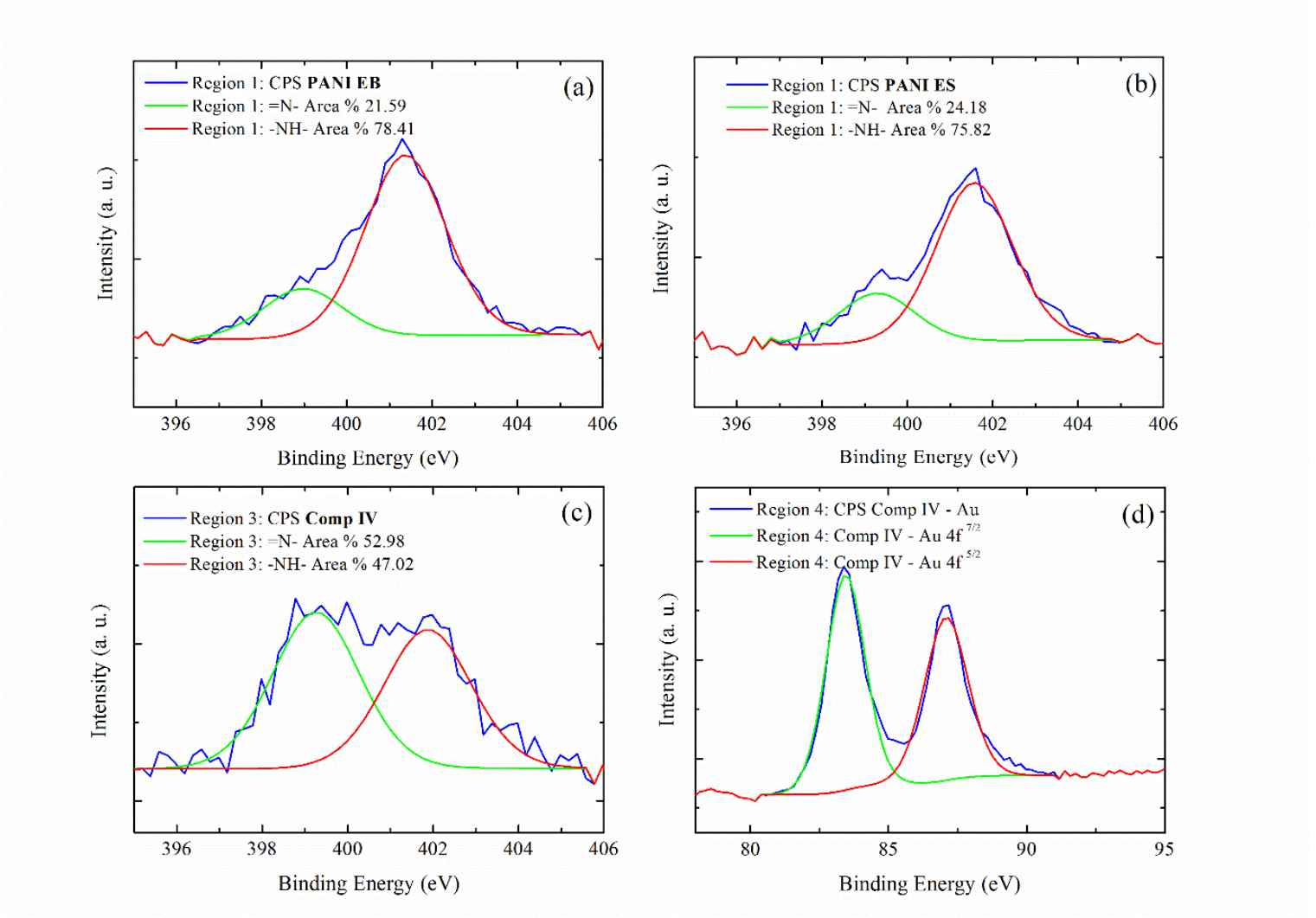
Region 1: CPS PANI EB
Region 1: =N- Area % 21.59
Region 1: -NH- Area % 78.41
(a)
Intensity (a. u.)
396
398
400
402
404
406
Binding Energy (eV)
Region 1: CPS PANI ES
Region 1: =N- Area % 24.18
Region 1: -NH- Area % 75.82
(b)
Intensity (a. u.)
396
398
400
402
404
406
Binding Energy (eV)
Region 3: CPS Comp IV
Region 3: =N- Area % 52.98
Region 3: -NH- Area % 47.02
(c)
Intensity (a. u.)
396
398
400
402
404
406
Binding Energy (eV)
Region 4: CPS Comp IV - Au
Region 4: Comp IV - Au 4f 7/2
Region 4: Comp IV - Au 4f 5/2
(d)
Intensity (a. u.)
80
85
90
95
Binding Energy (eV)

Figure 3

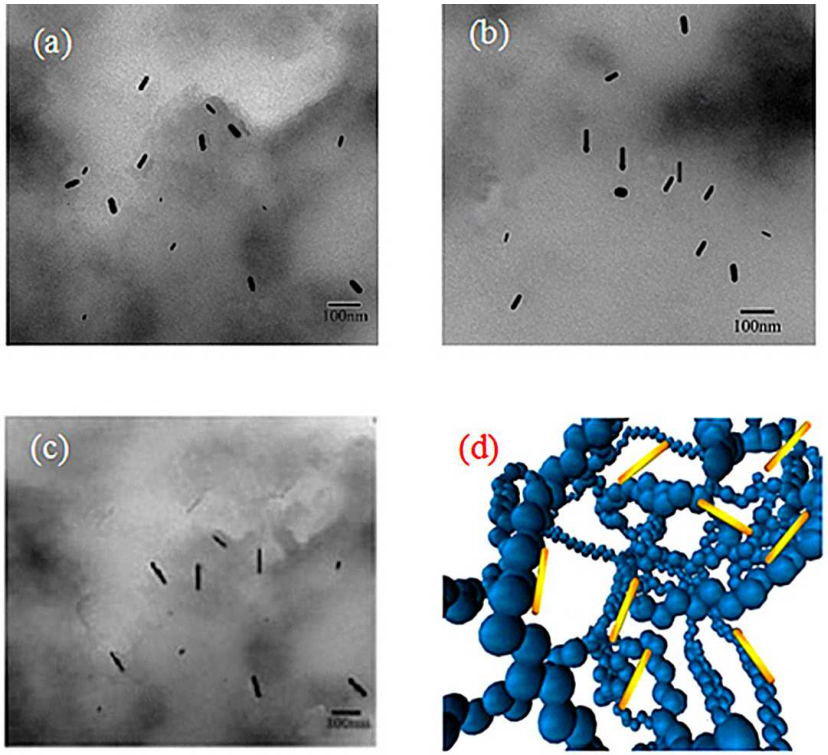

Figure 4

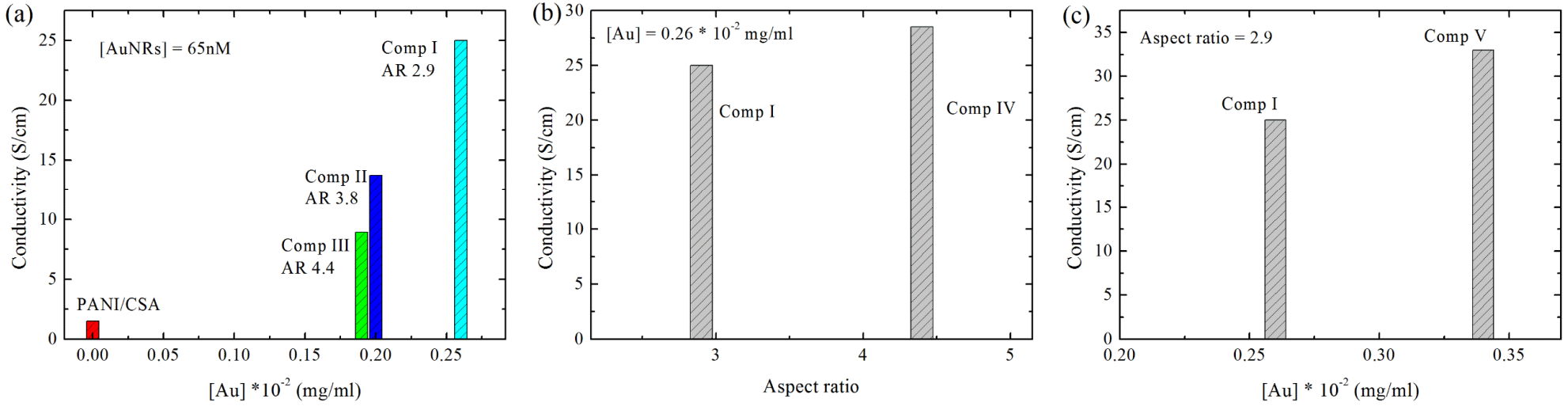
(a)
[AuNRs] = 65nM
Comp I
AR 2.9
Comp II
AR 3.8
Comp III
AR 4.4
PANI/CSA
Conductivity (S/cm)
[Au] *10-2 (mg/ml)
(b)
[Au] = 0.26 * 10-2 mg/ml
Comp I
Comp IV
Conductivity (S/cm)
Aspect ratio
(c)
Aspect ratio = 2.9
Comp I
Comp V
Conductivity (S/cm)
[Au] * 10-2 (mg/ml)

Figure 5

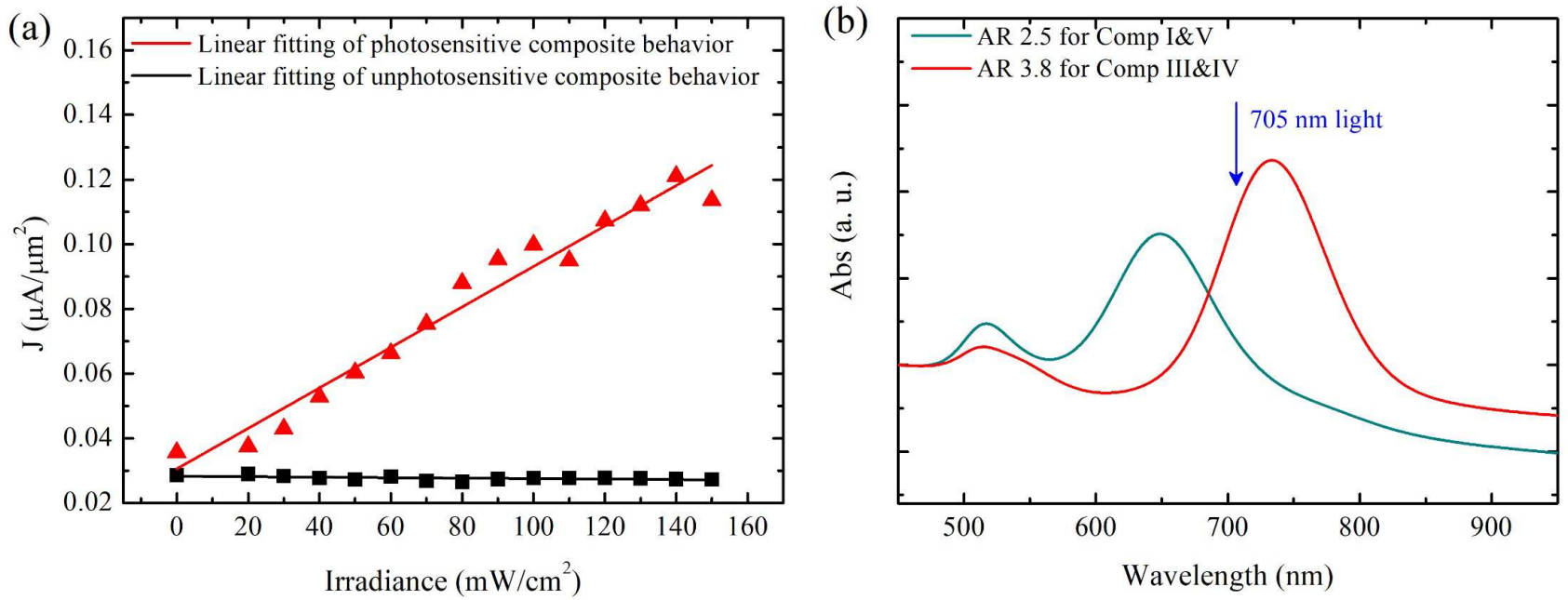
(a)
Linear fitting of photosensitive composite behavior
Linear fitting of unphotosensitive composite behavior
J (μA/μm²)
Irradiance (mW/cm²)
0.02
0.04
0.06
0.08
0.10
0.12
0.14
0.16
0
20
40
60
80
100
120
140
160
(b)
AR 2.5 for Comp I&V
AR 3.8 for Comp III&IV
705 nm light
Abs (a. u.)
Wavelength (nm)
500
600
700
800
900

Figure 6

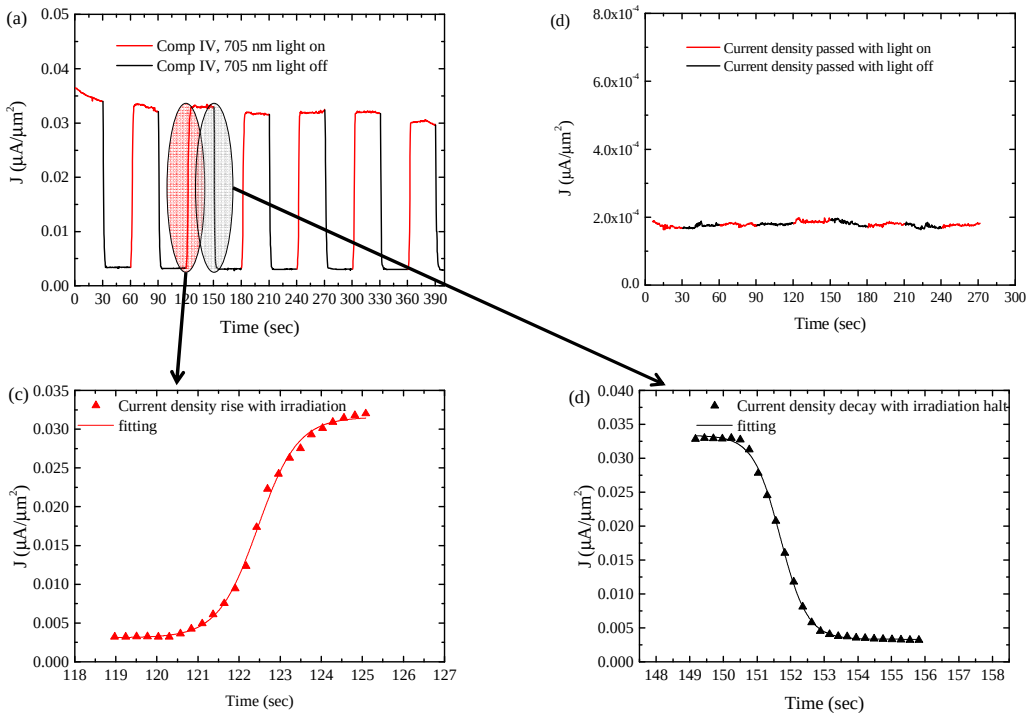

Figure 7

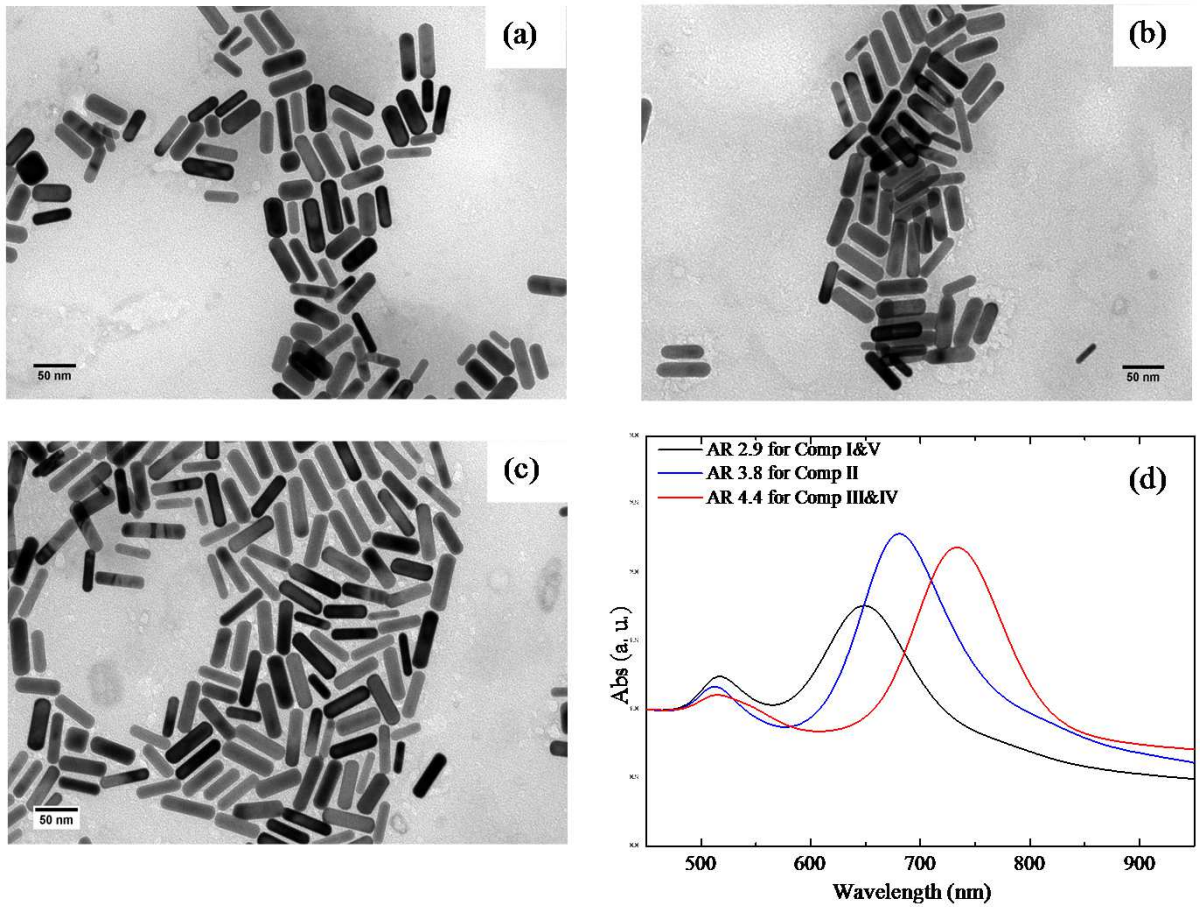
(a)
50 nm
(b)
50 nm
(c)
50 nm
(d)
AR 2.9 for Comp I&V
AR 3.8 for Comp II
AR 4.4 for Comp III&IV
Abs (a.u.)
500
600
700
800
900
Wavelength (nm)

Figure S1

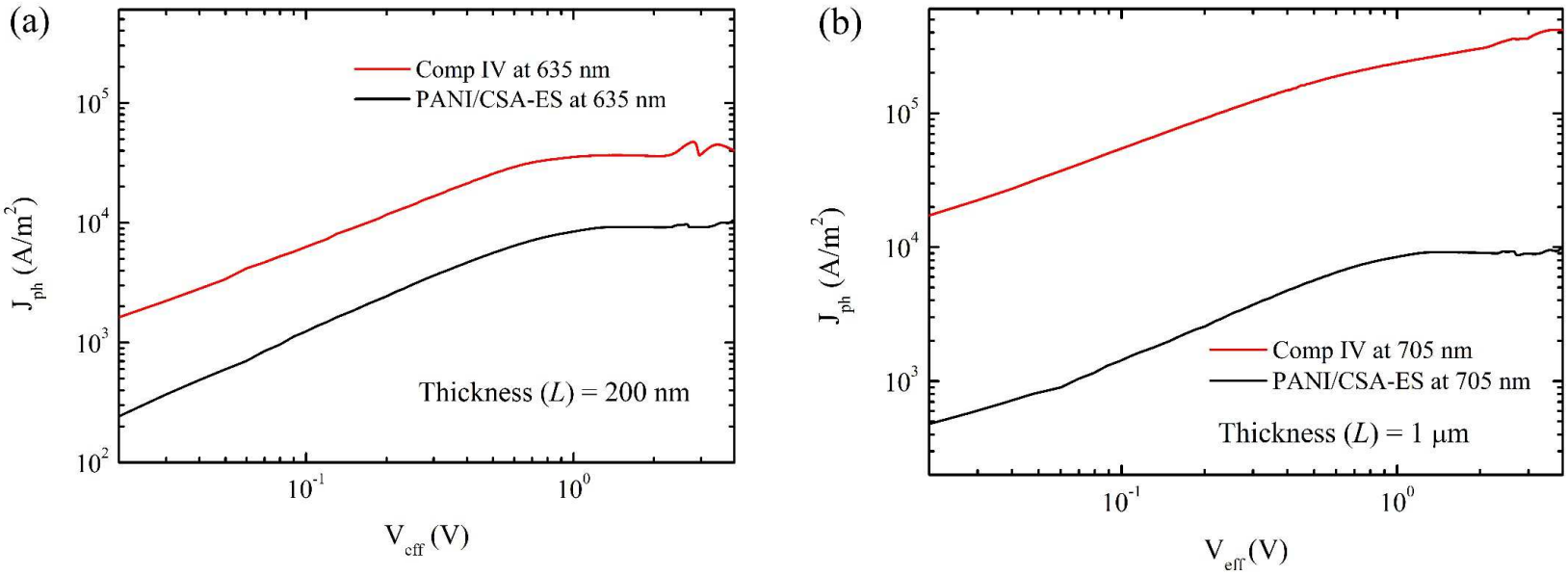
(a)
Comp IV at 635 nm
PANI/CSA-ES at 635 nm
Thickness (L) = 200 nm
J_ph (A/m^2)
V_eff (V)
(b)
Comp IV at 705 nm
PANI/CSA-ES at 705 nm
Thickness (L) = 1 μm
J_ph (A/m^2)
V_eff (V)

Figure S2